Article

Coherence Properties of a Supercontinuum Generated by Cascade Raman Processes in a Hollow-Core Fiber Filled with a Mixture of Deuterium and Hydrogen

Yury Yatsenko, Andrey Pryamikov * and Alexey Gladyshev

Prokhorov General Physics Institute of the Russian Academy of Sciences, Dianov Fiber Optics Research Center, 38 Vavilov Str., 119333 Moscow, Russia; yuriya@fo.gpi.ru (Y.Y.); alexglad@fo.gpi.ru (A.G.)
* Correspondence: pryamikov@fo.gpi.ru

Abstract: Here, we report a numerical study of supercontinuum generation in an antiresonant optical fiber with a hollow core filled with a mixture of deuterium (D_2) and hydrogen (H_2). For 1 ps pulses at a wavelength of 1.03 μm with different chirp values, we demonstrate a possibility of obtaining a mid-IR coherent supercontinuum with a spectral width of 2300 nm, initiated by cascade processes at resonance frequencies of vibrational and rotational levels of D_2 and H_2. We show that an increase in the chirped pulse duration to 25 ps while maintaining the energy and spectral width allows increasing the quantum conversion efficiency in the mid-IR from 10 to 50% and expanding the range of optimal fiber lengths at which a high degree of supercontinuum coherence is achieved.

Keywords: coherent supercontinuum; gas-filled hollow-core fiber; stimulated Raman scattering

1. Introduction

A mid-IR coherent supercontinuum is in demand for many applications such as biomedicine [1–3], mid-infrared optical coherence tomography [4,5], and remote sensing [6]. A promising way to obtain a supercontinuum in the important molecular "fingerprint" mid-IR range of 2–5 μm is the generation of cascade Stokes shifts of stimulated Raman scattering (SRS) in a gas-filled optical fiber by high-power picosecond and femtosecond lasers in the near-IR range [7–12]. Recently, antiresonant hollow-core fibers (HCF) [13–19] have been intensively used for this purpose. They have wide transmission bands in the wavelength range from UV to mid-IR, and in each of them, the dispersion characteristic passes through zero values. This not only increases the efficiency of cascade SRS at resonant frequencies falling in the region of low band losses but also significantly expands the possibilities of fulfilling a phase-matching condition for nonlinear four-photon processes that effectively broaden the spectrum in the Stokes-anti-Stokes regions.

An increase in the energy conversion to the mid-IR was demonstrated in [10–12], where cascade SRS was used at vibrational levels of light gases, the large frequency shifts of which fell into the low loss regions of transmission bands. In experimental works [10,12], three transmission bands of an HCF were used to obtain mid-IR generation in a two-stage process 1.03 → 1.49 → 2.68 μm at D_2 vibrational levels. When pumping with the 10 ps pulses with a chirp value C = 40, a transform-limited pulse of 920 fs with a quantum conversion efficiency (the total number of photons entering a given spectral region to the number of photons of the input pump pulse) of 28% was obtained in the second Stokes [10]. Reducing the input pulse duration to 1 ps while maintaining its spectral width (C = 4) led to supercontinuum generation in the wavelength range of 0.65–3.3 μm, yet in the range >2 μm, the quantum conversion efficiency was only 14% [11]. This was explained by an increasing role of Kerr nonlinear processes, which redistribute the pump energy into the short-wave (anti-Stokes) spectral region.

The role of Raman processes in the supercontinuum generation in the mid-IR range can be enhanced by using a mixture of gases that increase the number of resonant vibrational transitions involved in the transfer of energy to the Stokes regions [12,20]. The use of a D_2-H_2 mixture in the work [12], where, in addition to the two-stage process on D_2, combined two-stage processes of $1.03 \rightarrow 1.49 \rightarrow 3.9$ μm and $1.03 \rightarrow 1.8 \rightarrow 3.9$ μm were realized, made it possible to expand the supercontinuum spectrum in the mid-IR range to 4.2 μm. As in [11], a broadband supercontinuum was obtained with input chirped pulses of duration <1.5 ps, the spectral width of which corresponds to a transform-limited pulse of 250 fs. Increasing the chirped pulse duration to 12 ps while maintaining the energy led to an increase in the efficiency of conversion to the mid-IR, but in this case the spectrum had a strong modulation at the SRS resonance frequencies.

To increase the coherence of the supercontinuum initiated by the Raman process, it is preferable to have input pulses with the widest possible spectrum, overlapping the spectral Stokes shift. However, at large Raman shifts of the vibrational levels of molecular gases (125 THz for H_2), this requires transform-limited pulses of the order of femtoseconds. A promising way to increase coherence is to use combined cascade transitions involving vibrational and rotational levels, which have much smaller Stokes shifts. In [20], it was shown that the use of a single-cascade vibrational transition in D_2 (1.56–2.9 μm) and rotational transitions in N_2 in a D_2-N_2 mixture increased the degree of supercontinuum coherence and the maximum values of the quantum efficiency of Raman conversion to the three-micron wavelength region compared to a single-cascade process in deuterium.

It should be noted that the research carried out to date is not yet sufficient to fully realize all the possibilities of this method of generating a supercontinuum. Thus, the problem of obtaining high-energy single-period pulses in the mid-IR range when implementing cascade SRS processes in a gas-filled fiber has not been solved experimentally. Due to the complex nature of the interaction between SRS and Kerr nonlinearity in cascade processes, the question of whether it is possible to simultaneously obtain high efficiency of energy conversion from the near to mid-IR range and a perfect coherence of the supercontinuum, covering the 2–5 μm band, remains unclear.

In this paper, we numerically investigate the coherence properties of the supercontinuum formed by combined cascade Raman processes in a revolver-type HCF filled with a D_2-H_2 mixture pumped by chirped picosecond pulses at a wavelength of 1.03 μm. We examine the dependence of the spectrally averaged coherence and quantum conversion efficiency on the energy, duration, and chirp value of the input pulses and the fiber length. The fiber lengths and pulse parameters are determined, at which point it is possible to obtain a perfect phase coherence of the supercontinuum in the mid-IR. It is shown that taking into account the rotational transitions of D_2 and H_2 significantly expands the region of optimal pulse and fiber parameters in which a high degree of supercontinuum coherence is achieved.

2. Materials and Methods

The numerical analysis was carried out on the basis of the generalized nonlinear Schrödinger equation for the complex spectral pulse envelope [21], in which the total Raman response function $R(t)$ has the form [22,23] of

$$R(t) = R_{vibD2}(t) + R_{vibH2}(t) + R_{rotD2}(t) + R_{rotH2}(t) \qquad (1)$$

where the nonlinear response functions of deuterium $R_{vibD2}(t)$ and hydrogen $R_{vibH2}(t)$ were expressed as

$$R_{vib}(t) = (1 - f_{vib})\delta(t) + f_{vib}h_{vib}(t) \qquad (2)$$

Here, the first term with the delta function is responsible for the Kerr effect; the second term characterizes the contribution value of the more slowly relaxing vibrational response

of deuterium ($Q_1(2) = 2987$ cm^{-1}) or hydrogen ($Q_1(1) = 4155$ cm^{-1}). The SRS response function of deuterium and hydrogen $h_{vib}(t)$ was determined as

$$h_{vib}(t) = \Omega^2 \tau_{svib} \exp\left(-\frac{t}{\tau_{dvib}}\right) sin\left(\frac{t}{\tau_{svib}}\right) \qquad (3)$$

where $\Omega^2 = \tau_{svib}^{-2} + \tau_{dvib}^{-2}$, $\tau_{svib} = 1/\omega_R$, ω_R—is the angular frequency of the Raman shift; $\tau_{dvib} = T_2$, T_2 is the transverse relaxation time of the excited vibrational level. When determining T_2 for deuterium and hydrogen, the linewidth dependence of the Raman vibrational transition $\Delta\nu_R$ on the particle number density ρ given in [24] was taken into account ($\Delta\nu_R[D_2] = 101/\rho + 120*\rho$, $\Delta\nu_R[H_2] = 309/\rho + 51.8*\rho$).

The nonlinear function for rotational SRS in deuterium $R_{rotD2}(t)$ and hydrogen $R_{rotH2}(t)$ has a similar form

$$R_{rot}(t) = (1 - f_{rot})\delta(t) + f_{rot}h_{rot}(t) \qquad (4)$$

where the function $h_{rot}(t)$, characterizing the total contribution of 4 S_0-components of rotational SRS in hydrogen and deuterium to the nonlinear refractive index, is defined as

$$h_{rot}(t) = \sum_J A_J \exp\left(-\frac{t}{\tau_{drot}(J)}\right) sin\left(\frac{t}{\tau_{srot}(J)}\right), \qquad (5)$$

Here, $A_J = (N_{J+2} - N_J)q_J \frac{(J+2)(J+1)}{(2J+3)}$, $N_J = \exp\left[-\frac{hcBJ(J+1)}{KT}\right]$, $\tau_{srot}(J) = 1/[4\pi Bc(2J+3)]$, and $q_J = 1, 2$ for odd and even J, respectively. Here, K is the Boltzmann constant, T is the gas temperature, the rotational constant is $B = 29.3$ cm^{-1} in deuterium and $B = 59.8$ cm^{-1} in hydrogen, A_J characterizes the intensity of the rotational transition $\omega_J = 2Bc(2J+3)$, determined by the selection rules $\Delta J = \pm 2$, with the energy $E_J = J(J+1)Bhc$, where h– is Planck's constant. N_J and $\tau_{drot}(J)$ are the population of gas molecules at level J and the time of its transverse relaxation, depending on the gas temperature and pressure [22,25]. The coefficients f_{vib}, f_{rot}, characterizing the SRS contribution to the value of the nonlinear refractive index N_2 were determined in accordance with the work [26].

The numerical analysis was performed in the MATLAB environment for the fundamental mode of the fiber, taking into account the spectral dependences of the effective mode area $A_{\text{eff}}(\omega)$, waveguide losses $\alpha(\omega)$, and the effective refractive index. The maximum time interval was 120 ps with a minimum grid size of 0.46 fs. The study was carried out for input positively chirped Gaussian pulses with an amplitude $E(t) = \sqrt{P}\exp\left\{-0.5(1 + iC)[t/T_0]^2\right\}$, where P is the power, $\tau_{FWHM} = 1.665T_0$ is the full width at a half-maximum, and C is the chirp value. The main results were obtained for 1 ps chirped pulses with $C = 4$ and $C = 20$ and for longer 25 ps chirped pulses with $C = 100$ in the energy range of 1–500 μJ. All results were obtained at partial pressures of deuterium of 12 atm and hydrogen of 20 atm, at which the maximum conversion efficiency values were achieved in the experiment [12] in combined two-cascade processes (1.03–1.49–3.9 μm and 1.03–1.8–3.9 μm) involving the vibrational transition of deuterium at 2987 cm^{-1} (1.03–1.49 μm) and hydrogen at 4155 cm^{-1} (1.03–1.8 μm). The supercontinuum generation was investigated both for the case of a purely vibrational Raman process and with the participation of, along with vibrational rotational levels in D_2 and H_2.

To estimate the degree of coherence depending on the wavelength, a first-order correlation function $\left|g_{12}^{(1)}(\lambda)\right|$ was used [27]. The ensemble average of 380 independent pairs of spectral amplitudes $E(\lambda)$ was determined from 20 individual realizations of supercontinuum with different phase noise. Quantum noise was introduced additively to the amplitude of the input pulse with an amplitude corresponding to one photon in the frequency interval and a random phase. The supercontinuum coherence in different parts of the spectrum was estimated using the spectrally averaged correlation function $<\left|g_{12}^{(1)}(\lambda)\right|> = \int \left|g_{12}^{(1)}(\lambda)\right| |E(\lambda)|^2 d\lambda / \int |E(\lambda)|^2 d\lambda$.

Numerical analysis was performed for parameters of the 10-capillary HCF with a core diameter of 75 μm and a capillary wall thickness of 1.15 μm (Figure 1a) corresponding to the manufactured HCF used in experiments [11,12]. The dispersion and waveguide characteristics are shown in Figure 1b. The supercontinuum was studied in the range of 500–5000 nm, covering the first 5 transmission bands of the optical fiber. The wavelengths of the pump (1.03 μm), the first Stokes shifts in deuterium (1.49 μm) and hydrogen (1.8 μm), and the two-cascade shifts of 2.6 μm and 3.9 μm were in the region of minimal losses of the 3rd, 2nd, and 1st transmission bands, respectively.
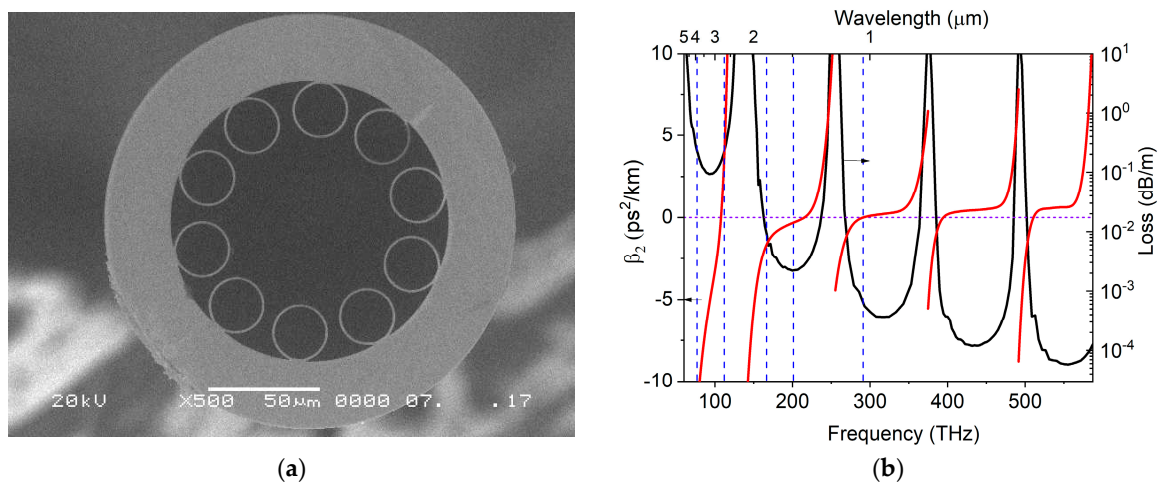

(**a**)   (**b**)

Figure 1. (**a**) Electron photograph of the fiber cross-section; (**b**) Waveguide (leakage) loss (black) and dispersion (red) of the fundamental mode as a function of wavelength at partial pressures of deuterium of 12 atm and hydrogen of 20 atm for 5 transmission bands. The vertical dashed lines denote the wavelengths of the pump (1.03 μm), the first Stokes shifts in deuterium (1.49 μm) and hydrogen (1.8 μm), and the two-cascade shifts of 2.6 μm and 3.9 μm. The horizontal line (dots) indicating the zero-dispersion value.

3. Results

3.1. Chirped Pulses of 1 ps Duration

3.1.1. Supercontinuum Generation upon Excitation of Vibrational Levels in D_2 and H_2

Figures 2 and 3 show the spectral and temporal characteristics obtained for 1 ps pulses with a chirp of C = 4 and C = 20 at an energy of 200 μJ. These pulses differ greatly in their spectral width (FWHM is 60.6 cm^{-1} and 294.6 cm^{-1}, respectively). Supercontinuum generation begins with the smooth broadening of the spectrum by self-phase modulation (SPM), which at lengths of 0.5–0.7 m is replaced by a very fast spectrum broadening into the Stokes-anti-Stokes regions, forming a supercontinuum filling the entire wavelength range of 500–5000 nm (Figures 2a and 3a). This supercontinuum formation is characteristic of pulses with a spectrum corresponding to transform-limited pulses of femtosecond duration [27], when the dominant role in the uniform distribution of energy in the supercontinuum spectrum is played by coherent processes associated with the SPM, cross-phase modulation (XPM), the decay of a high-order soliton under the influence of higher dispersion and nonlinear terms, and stochastic four-wave processes associated with modulation instability. The role of Raman processes is manifested mainly in the transfer of energy into the long-wave region of resonant cascade transitions of deuterium and hydrogen 1.49, 1.8, 2.68, and 3.9 μm, as well as in the amplification of non-resonant nonlinear processes in this spectral region.

At the initial fiber lengths, the quantum conversion efficiency in the Stokes and anti-Stokes spectral regions is approximately the same (Figures 2b and 3b). Here, the broadening of the SPM spectrum is accompanied by increasing asymmetry in the spectrum and temporal structure and the occurrence of modulation at the pulse trailing edge (Figures 2c,d and 3c,d). Further sharpening of the modulation structure leads, at lengths greater than 0.7 m for the chirp C = 4 and 0.5 m for the chirp C = 20, to the decay of the

initial pulse shape into numerous soliton-like pulses, accompanied by a sharp broadening of the spectrum into the Stokes-anti-Stokes regions.

Due to the impact of Raman cascade processes, the quantum conversion efficiency in the Stokes IR spectral range (1030–5000 nm) is greater than in the anti-Stokes (510–1030 nm) along the entire length of the fiber. In this case, the initial sharp increase in the quantum conversion efficiency in the Stokes region to values >0.6 (IR curve) with the expansion of the spectrum to the wavelength region of the first Stokes components D_2 (1.49 μm) and H_2 (1.8 μm), corresponding to the near IR range, is accompanied by a decrease in the quantum conversion efficiency in the anti-Stokes region to values less than 0.3. Further energy transfer to the mid-IR region (2400–5000 nm), corresponding to the wavelengths of cascaded Raman scattering (2.68 μm, 3.9 μm), leads to an increase in the quantum conversion efficiency in the mid-IR to values of ~0.1 over a length of ~1.5 m (MIR curve), while the quantum conversion efficiency in the entire IR range decreases here to a value of <0.3 and in the anti-Stokes region <0.1. Thus, with maximum spectrum expansion into the mid-IR, more than 60% of photons are lost at the boundaries of the 5 used transmission bands of the fiber. As follows from the spectral and temporal characteristics shown in Figures 2 and 3 for 1 ps chirped pulses with C = 4 and C = 20, there is a significant difference in the rate of spectrum broadening by SPM. The large spectral width of the input chirped pulse with C = 20 provides spectrum broadening sufficient for forming the supercontinuum modulation structure on a shorter (by 20 cm) fiber length. This is of decisive importance for obtaining a coherent supercontinuum with chirp C = 20. The main process negatively affecting the coherent properties is modulation instability associated with four-photon nonlinear processes that amplify spontaneous noise, which manifests itself already at the earliest stages of the SPM spectrum broadening. Numerical analysis of the phase matching condition ($2\beta_P - \beta_S - \beta_{AS} + 2\gamma P = 0$, where β_P, β_S and β_{AS} are propagation constants for pump, Stokes and anti-Stokes waves, γ is the nonlinear coefficient, P is the pump power) for the four-wave process ($2\omega_P = \omega_S + \omega_{AS}$) showed that when pumping with 200 MW pulses at a wavelength of 1.03 μm, located in the third band near the zero dispersion wavelength (λ_0 = 1.29 μm), the phase matching condition is satisfied for the Stokes-anti-Stokes shifts at wavelengths of 1178 and 895 nm, located in the second and third transmission bands of the fiber, and at wavelengths of 651 and 2465 nm, belonging, respectively, to the fourth and first transmission bands. Thus, the exponential gain $g_{MI} = \gamma P$ in the region of these wavelengths leads to a noticeable development of stochastic processes at the length $L_{MI} = 16/\gamma P$ = 17 cm (γ = 4.7 × 10^{-7} m^{-1} W^{-1}, P = 200 MW). In particular, the formation of the modulation temporal structure begins with the appearance of periodic oscillations with a period of ~24–27 fs at the fiber lengths of 0.5–0.6 m (chirp C = 4) and 0.35–0.4 m (chirp C = 20) (Figures 2d and 3d). These harmonic oscillations correspond to the interference between the pump radiation of 1.03 μm and the radiation in the region of wavelengths of 895 and 1178 nm, arising already at these initial fiber lengths from the spontaneous noise in the process $2\omega_{1030} = \omega_{1178} + \omega_{895}$.

From the spectrograms in Figure 2c, which show superimposed spectra for 4 input pulses differing in random phase noise, it follows that for a chirped pulse with C = 4, the generation of radiation in the wavelength range of 895 and 1178 nm already leads to differences in their spectrum at lengths of <0.6 m, since, here, the rate of the SPM spectrum broadening lags behind the development rate of this noise nonlinear process. At the same time, the SPM fast-broadening rate of the broader-band spectrum of the chirped pulse with C = 20 suppresses the spontaneous process at the initial lengths of 0.1–0.4 m. The fast development of coherent cascade processes associated with a further decay of the envelope with the participation of Raman and higher dispersion terms for a chirped pulse with C = 20 leads to the effective suppression of the second noise process $2\omega_{1030} = \omega_{2465} + \omega_{651}$ also, which affects the coherence in the region of the second Stokes components (2.68 and 3.9 μm). This is evidenced by the absence of fluctuations in the spectrum for pulses with different phase noise up to a fiber length of 0.6–0.7 m, corresponding to the maximum spectrum broadening (Figure 3c). Figure 4 shows the degree of coherence of the supercontinuum

estimated using the first-order correlation function $\left|g_{12}^{(1)}(\lambda)\right|$, which shows a significantly higher supercontinuum coherence for a chirped pulse with C = 20 compared to a chirped pulse with C = 4. A significant difference in coherence between these chirp values is also manifested in the dependence of the spectrally averaged first-order correlation function $<\left|g_{12}^{(1)}(\lambda)\right|>$ on the energy of the input pulses (Figure 5). For the chirped pulse with C = 4, the values of $<\left|g_{12}^{(1)}(\lambda)\right|>$ in the mid-IR wavelength region (2.4–5 μm) are at a low level of 0.12–0.14 with a change in the pump energy, while for the chirped pulse with C = 20, the average coherence in this spectral range increases from 0.45 to 1 with an increase in energy from 60 to 200 μJ, thus demonstrating perfect phase coherence in the region of optimal fiber lengths at pumping energies greater than 150 μJ. The deterioration of the coherence with a decrease in the energy of the input pulse with the C = 20 chirp below 150 μJ is due to a decrease in the influence of the nonlinear term $2\gamma P$ and an increase in the role of waveguide dispersion. As a result, the number of wavelengths at which the phase-matching condition for noise processes is satisfied increases, which significantly complicates their suppression. In particular, for a pulse with a power of 60 MW there are 5 frequency offsets from the pump (47.5, 73, 104, 140 and 196.6 THz), where the generation from spontaneous noise is possible due to four-photon nonlinear processes.
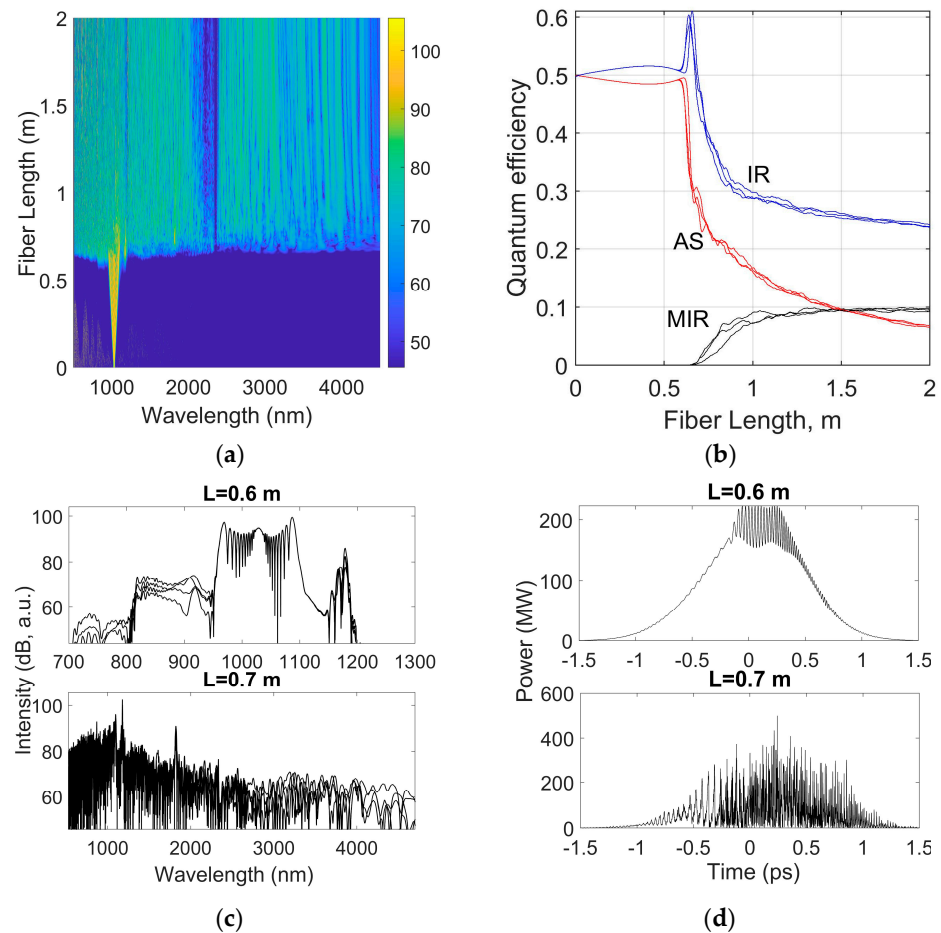

Figure 2. (**a**) Spectrum evolution of a 1 ps pulse (C = 4) with an energy of 200 μJ along the fiber length; (**b**) Quantum conversion efficiency in different spectral regions depending on the fiber length (here and in the following figures IR is the region of near- and mid-IR wavelengths 1.03–5 μm, MIR is the mid-IR region 2.4–5 μm, AS is the anti-Stokes region <1.03 μm); (**c**) Spectrum and (**d**) temporal structure at the initial fiber lengths. Only vibrational SRS transitions are taken into account.
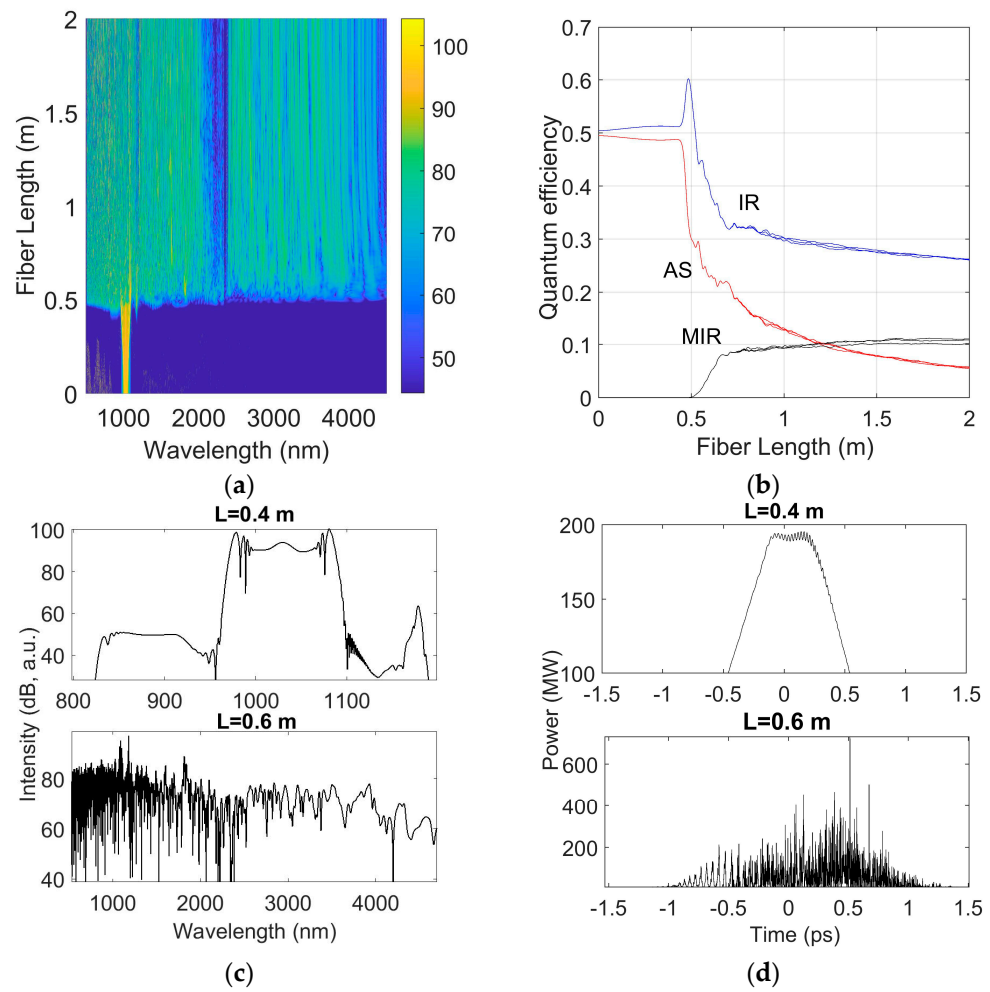
Figure 3. (**a**) Evolution of the spectrum of a 1 ps chirped pulse (C = 20) with an energy of 200 μJ along the fiber length; (**b**) Quantum conversion efficiency in different spectral regions depending on the fiber length; (**c**) Spectrum and (**d**) temporal structure at the initial fiber lengths. Only vibrational SRS transitions are taken into account.
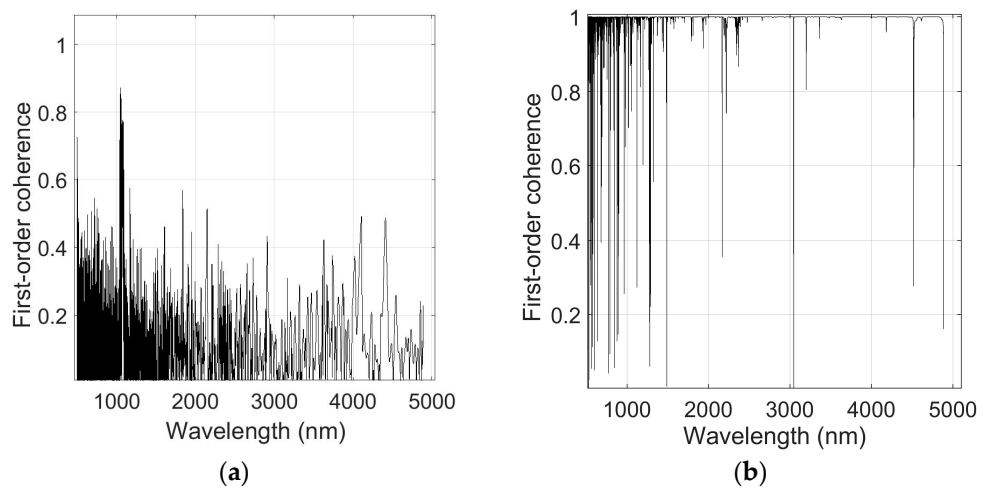

Figure 4. The degree of coherence of the supercontinuum in the wavelength range of 500–5000 nm with pumping at 1030 nm by 1 ps input chirped pulses with (**a**) C = 4 and (**b**) C = 20 taking into account vibrational transitions in D_2 and H_2. Pump energy is 200 μJ. The fiber length is 0.7 m.

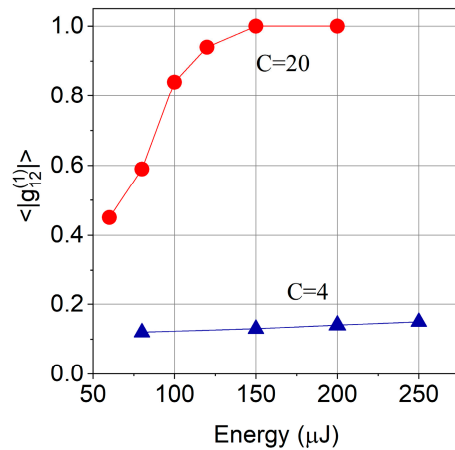**Figure 5.** Spectrally averaged coherence ($< \left| g_{12}^{(1)}(\lambda) \right| >$) in the mid-IR wavelength region (2.4–5 μm) depending on the energy of 1 ps input chirped pulses at 1.03 μm with C = 4 (triangles) and C = 20 (dots). Only vibrational transitions in D_2 and H_2 are taken into account.

Figure 6 shows how the quantum efficiency and spectral bandwidth in the mid-IR depend on the energy of 1 ps input chirped pulses with C = 4 (for 1 ps input chirped pulses with C = 20, these dependences differ insignificantly). At the maximum spectrum broadening, the quantum conversion efficiency in the long-wavelength region of 1030–5000 nm is at the level of ~30% and weakly depends on the energy in the range of 60–200 μJ. At the same time, the quantum conversion efficiency in the mid-IR (>2.4 μm) increases with increasing energy to a value of ~10% at an energy of 200 μJ. An increase in the mid-IR bandwidth (by a factor of 1.7) with increasing energy is accompanied by an almost 3-fold decrease in the optimal fiber length corresponding to the maximum broadening of the supercontinuum spectrum.
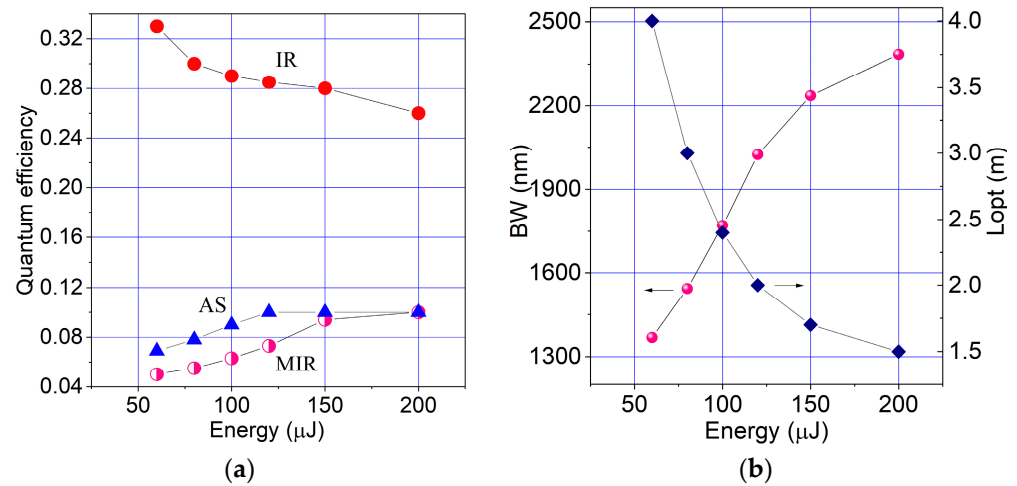

Figure 6. (**a**) Quantum conversion efficiency in different spectral regions at optimal fiber lengths corresponding to the maximum supercontinuum bandwidth; (**b**) Supercontinuum bandwidth (BW) in the mid-IR region >2.4 μm and optimal fiber length (Lopt) versus energy, when pumped at 1.03 μm with 1 ps chirped pulses (C = 4). Only D_2 and H_2 vibrational transitions are taken into account.

3.1.2. Supercontinuum Generation upon Excitation of Vibrational and Rotational Levels in D_2 and H_2

Under normal conditions of linearly polarized radiation for 1 ps chirped pulses with C = 4, having a narrow spectral width, the excitation thresholds of relatively far-spaced components of rotational SRS in hydrogen ($S_0(1) = 587$ cm^{-1}) and deuterium ($S_0(2) = 415$ cm^{-1}) are significantly higher than vibrational SRS in these gases [28]. In this regard, the contri-

bution of rotational SRS to the supercontinuum generation for such pulses depends to a greater extent on their energy.

From the results shown in Figure 7, for an input pulse energy of 200 μJ, it follows that the rotational levels did not significantly affect supercontinuum generation, determined by the large contribution of nonlinear four-wave processes, and only led to a shortening of the length (0.4 m), at which point a significant broadening of the SPM spectrum and decay of the envelope occur occur. In the studied energy range, the quantum conversion efficiencies in the mid-IR were also close to those obtained without taking into account the rotational levels (Figure 7b). The most important difference was found in the supercontinuum coherence (Figure 8). For a chirped pulse with C = 4, the value of $< \left| g_{12}^{(1)}(\lambda) \right| >$ increases from 0.2 to 1 in the mid-IR with a change in the pump energy from 40 to 250 μJ. For a chirped pulse with C = 20, $< \left| g_{12}^{(1)}(\lambda) \right| > = 1$ in this entire range of pump energies. A significant positive effect in the supercontinuum coherence from rotational SRS is associated with the fact that new rotational cascade processes, along with vibrational ones, compete with noise Kerr processes at the early stages of the SPM spectrum broadening. From the spectrogram obtained for a chirped pulse with C = 4 at an energy of 200 μJ (Figure 7a), it follows that at a length of 0.2 m, coherent broadening of the SPM spectrum already occurs, extending at the level of −60 dB into the long-wave range up to a wavelength of 1200 nm. Thus, the above-mentioned noise process with the Stokes shift, which has gain maxima at wavelengths of 895 nm and 1178 nm, is overlapped. The most probable mechanism of such accelerated spectrum broadening are cascade processes involving rotational transitions of $S_0(1)$ in hydrogen and $S_0(2)$ in deuterium.

Figure 8b shows how the spectrally averaged coherence in the mid-IR range, obtained for a 1 ps chirped pulse (C = 4) with an energy of 250 μJ, varied along the fiber length. Perfect phase coherence here exists only at short fiber lengths of up to 0.3 m, where the quantum conversion efficiency reaches 70–80% of its maximum value at 0.5 m. The sharp decrease in coherence shows that the maximum values of quantum efficiency are determined by noisy four-photon processes. This is a characteristic feature of all the chirped pulses of 1 ps duration considered above.
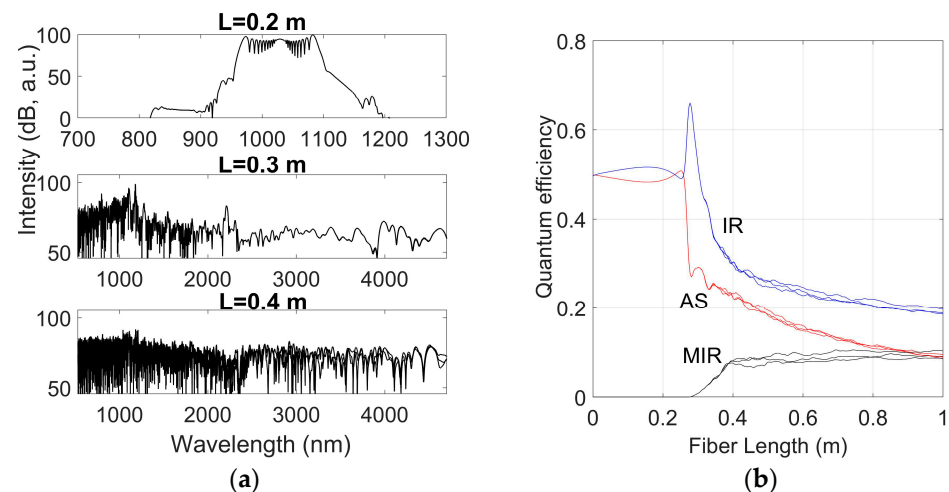

Figure 7. (**a**) Supercontinuum evolution at initial fiber lengths when launching a 1 ps chirped pulse (C = 4) with an energy of 200 μJ into the fiber; (**b**) Quantum conversion efficiency in different spectral regions depending on the fiber length. Vibrational and rotational transitions of SRS are taken into account.
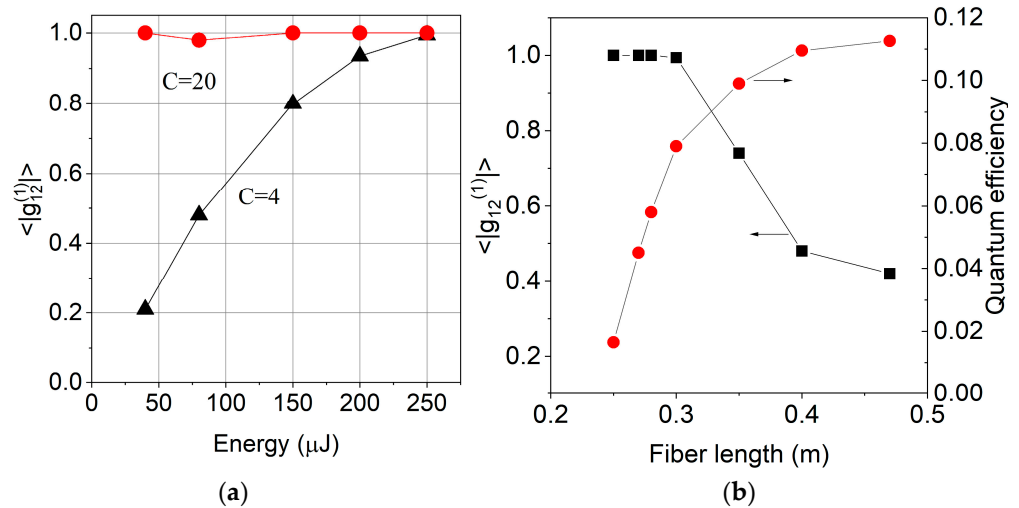
Figure 8. (**a**) Spectrally averaged coherence ($< \left| g_{12}^{(1)}(\lambda) \right| >$) in the mid-IR wavelength region (2.4–5 μm) dependent on the energy of 1 ps input chirped pulses at 1.03 μm with C = 4 (triangles) and C = 20 (dots); (**b**) Quantum conversion efficiency and spectrally averaged coherence in the Mid-IR obtained for 1 ps pulses (C = 4) with the energy of 250 μJ as a function of fiber length. Vibrational and rotational transitions in D_2 and H_2 are taken into account.

3.2. Chirped Pulses of 25 ps Duration

A numerical analysis was performed also for chirped pulses of 25 ps duration. With such duration, the Raman process still retains its non-stationarity and, accordingly, a high degree of coherence [29], while its role in the efficiency of energy conversion into the IR range becomes decisive. Figures 9 and 10 show results obtained for 25 ps input chirped pulses with C = 100 and an energy of 250 μJ on a fiber length of 2 m, taking into account only vibrational and vibrational-rotational levels in D_2 and H_2, respectively. These pulses have almost the same spectral width (58.8 cm^{-1}) as the 1 ps chirped pulses with C = 4 considered above. Comparison with similar spectra for a duration of 1 ps in this energy range (Figure 2) shows a noticeable difference in the supercontinuum evolution, associated with a significantly greater influence of SRS on the spectrum formation for a 25-ps pulse not only at the initial lengths, but also at the maximum of quantum efficiency.

Due to the lower peak power values and longer duration, the initial stage of supercontinuum generation is associated not with the SPM spectrum broadening, but with single- and double-cascade SRS processes, effectively transferring the pump energy to the long-wavelength region. At fiber lengths of 0.5–0.6 m, narrow Stokes signals of single-cascade processes in hydrogen and deuterium initially appear at 1.8 and 1.49 μm, which very quickly initiate the appearance of signals of two-cascade processes: a combined process at 3.9 μm and a two-cascade process in deuterium at 2.68 μm (Figures 9a and 10a). It is important to note that the envelope decay here begins with the formation of a regular modulation structure with a period of ~8 fs, which corresponds to the interference between the pump at 1.03 μm and the first Stokes signal in H_2 at 1.8 μm (Figure 9d). Almost simultaneously with the Stokes signals, as a result of coherent four-wave processes, signals also appear in the anti-Stokes region at wavelengths of 722 nm ($\omega_{0.72} = 2\omega_{1.03} - \omega_{1.8}$), 787 нм nm ($\omega_{0.78} = 2\omega_{1.03} - \omega_{1.49}$), 641 нм nm ($\omega_{0.64} = 2\omega_{1.03} - \omega_{2.6}$), and 593 нм nm ($\omega_{0.59} = 2\omega_{1.03} - \omega_{3.9}$). The interaction between these radiations leads to a rapid increase in the number of Stokes-anti-Stokes satellites. In contrast to the 1 ps pulse, where, due to the SPM broadening, these SRS processes developed against the background of the envelope decay into a modulation structure consisting of a large number of femtosecond pulses interacting with each other via four-wave processes; here, the SRS transformation into the long-wave region of the spectrum occurs at the stage when the modulation structure is not yet fully formed. This leads to a more efficient energy transfer to the mid-IR by cascade processes of vibrational SRS. The maximal values of conversion efficiency into the

mid-IR are achieved at a length of ~1 m and is 40% at an input energy of 250 μJ, while 30% and 16% of photons are in the near-IR and in the anti-Stokes region, respectively (Figures 9b and 10b). The dependence of the maximum values of the quantum efficiency on the pump energy, obtained for a 25 ps chirped pulse with C = 100 taking into account rotational SRS (Figure 10c), shows that at an energy of 125 μJ (power of 5 MW), 80% of the pump quanta can be transferred to the Stokes region of the spectrum, the majority (50%) of which is in the mid-IR range (>2.4 μm).
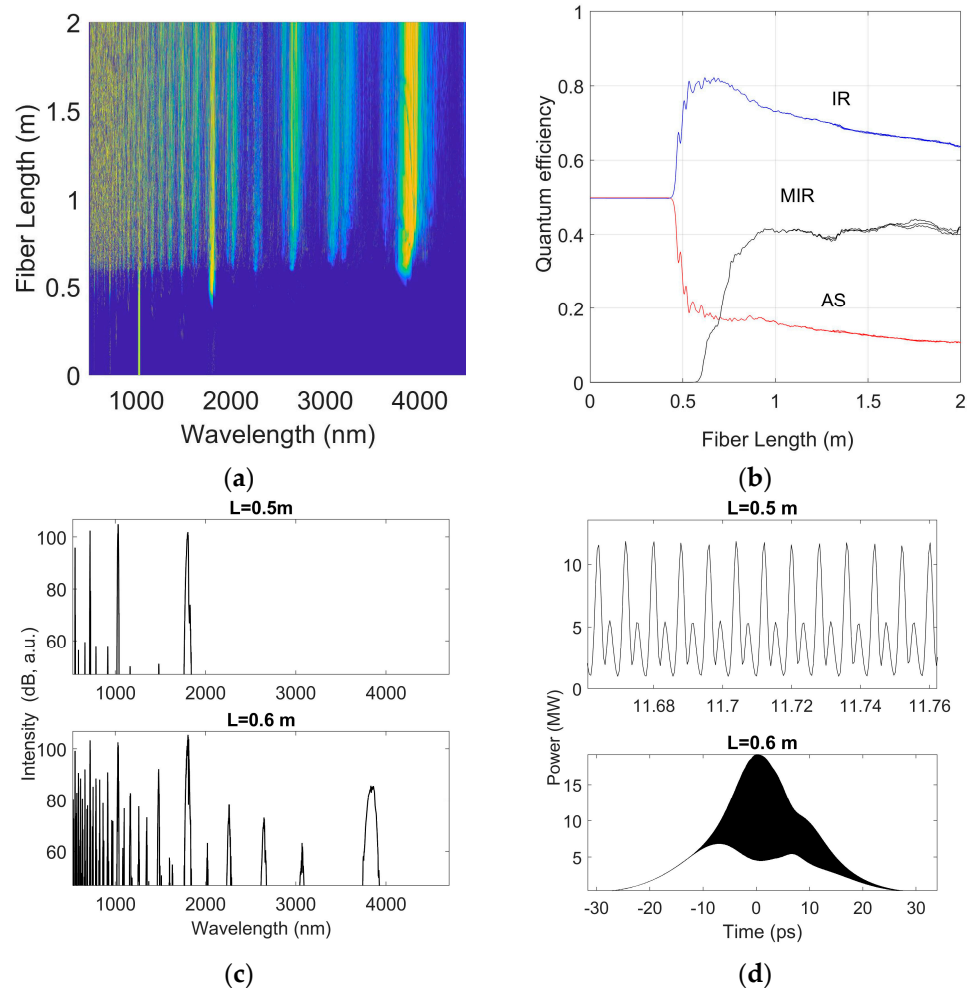

Figure 9. (**a**) Spectrogram and (**b**) quantum efficiency obtained for 25 ps input chirped pulses with C = 100 and an energy of 250 μJ on a 2 m optical fiber length; (**c**) Spectrum and (**d**) temporal structure at the initial fiber lengths. Only vibrational SRS transitions are taken into account.

It is important to note that the maximum values of the quantum conversion efficiency are determined by coherent nonlinear processes that successfully suppress the noise Kerr processes. This follows from the values of $< \left| g_{12}^{(1)}(\lambda) \right| >$ (Figure 10d) calculated at different fiber lengths for the spectrum shown in Figure 10a. In the mid-IR region, $< \left| g_{12}^{(1)}(\lambda) \right| > = 1$ over the 2-m fiber length, while 100% coherence in the entire spectral range of 500–5000 nm is maintained up to a length of 1.2 m. Thus, compared to 1-ps pulses (Figure 8b), the range of optimal lengths at the maximum of the quantum conversion efficiency, at which a perfect coherence of the supercontinuum can be obtained, is significantly expanded here. The gain in the quantum conversion efficiency and coherence for the 25 ps pulse compared to the 1 ps pulse in the studied range of energies and spectral widths is obtained at a significantly higher modulation of the supercontinuum spectrum. It follows from the oscillograms in Figures 9 and 10 that the supercontinuum spectrum consists of 27–29 broadened maxima,

spaced from each other by ~17–20 THz and distributed in the frequency range of more than three octaves. The position of the maxima and their detuning are determined by the resonant frequencies of the Stokes shifts on the vibrational transitions in D_2 and H_2, interacting with each other through four-photon processes. In particular, the mid-IR maximum at 3.1 μm, spaced by 17 THz from the resonant peaks at 2.68 μm and 3.9 μm, is formed as a result of the degenerate process $2\omega_{3.1} = \omega_{2.68} + \omega_{3.9}$. Comparison of the oscillograms in Figures 9 and 10, given, respectively, for purely vibrational and vibrational-rotational SRS, shows a significantly smaller modulation in the supercontinuum spectrum when taking into account rotational SRS. In particular, for the spectrum in Figure 9, the difference in intensity between the peak maximum at 3.9 μm and the minimum at 3.5 μm is about 40 dB at a fiber length of 2 m, whereas in the spectrum in Figure 10, this difference decreases to 20 dB. The modulation depth decreases with increasing fiber length and pulse power. However, obtaining a smoother spectrum is accompanied by an increase in losses at the boundaries of the fiber transmission bands and a decrease in the efficiency of energy conversion to the mid-IR range (Figure 10c).
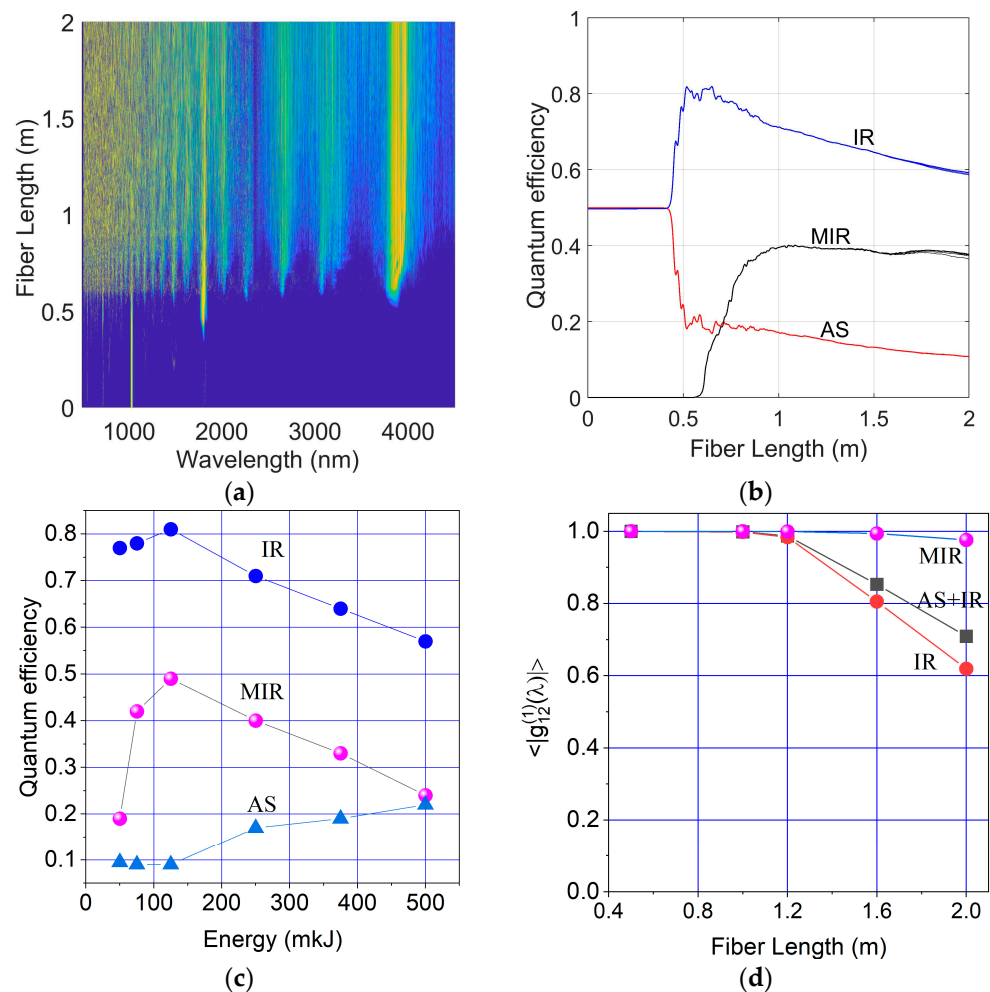

Figure 10. (**a**) Spectrogram and (**b**) quantum conversion efficiency obtained for 25 ps input pulses with a chirp of C = 100 and an energy of 250 μJ on a 2 m optical fiber length; (**c**) Dependence of the quantum conversion efficiency in the Stokes-anti-Stokes regions of the spectrum on the energy of the input pulse; (**d**) Dependence of the spectrally averaged coherence in different parts of the spectrum on the length of the fiber at an energy of 250 μJ. The duration of the input pulse is 25 ps, chirp C = 100. Vibrational and rotational transitions of SRS are taken into account.

4. Discussion

We have shown numerically the possibility of obtaining a perfectly coherent supercontinuum in the mid-IR range of 2–5 μm in a gas-filled hollow-core fiber pumped by chirped picosecond pulses at 1.03 μm when implementing a combined cascade Raman processes on vibrational and rotational levels of deuterium and hydrogen.

For a 1-ps chirped pulse with C = 20, a perfectly coherent supercontinuum can be obtained with a purely vibrational SRS process at pump energies, exceeding 150 μJ and fiber lengths <1 m. For a 1 ps narrower-band chirped pulse with C = 4, a perfect coherence of a supercontinuum is possible at pump energies more than 200 μJ only when using, along with the vibrational ones, the rotational levels in D_2 and H_2. The spectral width of such pulses allows coherent excitation of rotational levels in D_2 and H_2, enhancing the influence of coherent four-wave processes on supercontinuum generation. Excitation of the rotational levels improves the coherence properties of a supercontinuum for a 25 ps input chirped pulse as well, significantly extending the coherent length of the fiber at the maximal values of quantum conversion efficiency in the mid-IR.

Transfer of pump energy by two-cascade SRS processes to the mid-IR is accompanied by the formation of a femtosecond modulation structure in the pulse envelope and supercontinuum generation in the 500–5000 nm region. The share of energy in the mid-IR depends on which competing nonlinear processes determine its maximum values. For chirped pulses of 1 ps, the maximum values of the conversion efficiency in the mid-IR range are determined by four-wave parametric processes distributing the pump energy in the Stokes and anti-Stokes regions of the spectrum. The role of SRS is manifested at the initial stages in the initiation of a coherent modulation structure and in the amplification of parametric processes at resonance frequencies. While generating this continuous spectrum distributed over five transmission bands of the fiber, a significant part of the pump photons is absorbed at the boundaries of the transmission bands. The maximum values of quantum conversion efficiency in the IR range were 30% and only 10% were in the mid-IR range. This result is consistent with the experimentally obtained values in [12].

The numerical analysis showed that it is possible to significantly increase the pump energy conversion to the mid-IR and reduce energy losses at the transmission bands boundaries by increasing the duration of a chirped pulse while maintaining its energy. For a 25 ps chirped pulse with C = 100 at an energy of 125 μJ, the quantum conversion efficiency in the IR range was 80%, with 50% of the pump photons being in the mid-IR range. Here, with a lower power of the input pulses, SRS plays a major role not only in initiating the supercontinuum, but also in forming the maximum values of pump energy conversion to the mid-IR. A distinctive feature of a supercontinuum generated by a 25 ps pulse is an increased modulation of the spectrum, depending on the input power.

In conclusion, our new numerical results show that the implementation of cascade Raman processes on vibrational and rotational levels of hydrogen and deuterium in a gas-filled antiresonant optical fiber is promising for experimental realization of a coherent supercontinuum with a bandwidth that allows the generation of high-energy single-cycle pulses in the mid-IR region of 2–5 μm.

Author Contributions: Conceptualization, A.G. and Y.Y.; methodology, Y.Y.; software, Y.Y. and A.P.; validation, Y.Y., A.G. and A.P.; formal analysis, Y.Y. and A.P.; investigation, Y.Y.; resources, A.P.; data curation, A.G.; writing—original draft preparation, Y.Y.; writing—review and editing, Y.Y., A.G. and A.P.; visualization, Y.Y.; supervision, Y.Y. and A.G.; project administration, A.G. and A.P.; funding acquisition, A.P. and A.G. All authors have read and agreed to the published version of the manuscript.

Institutional Review Board Statement: Not applicable.

Informed Consent Statement: Not applicable.

Data Availability Statement: The data that support the findings of this study are available from the corresponding author, A.P., upon reasonable request.

Conflicts of Interest: The authors declare no conflicts of interest.

References

1. Petersen, C.R.; Prtljaga, N.; Farries, M.; Ward, J.; Napier, B.; Lloyd, G.R.; Nallala, J.; Stone, N.; Bang, O. Mid-infrared multispectral tissue imaging using a chalcogenide fiber supercontinuum source. *Opt. Lett.* **2018**, *43*, 999–1002. [CrossRef]
2. Pupeza, I.; Huber, M.; Trubetskov, M.; Schweinberger, W.; Hussain, S.A.; Hofer, C.; Fritsch, K.; Poetzlberger, M.; Vamos, L.; Fill, E.; et al. Field-resolved infrared spectroscopy of biological systems. *Nature* **2020**, *577*, 52–59. [CrossRef] [PubMed]
3. Borondics, F.; Jossent, M.; Sandt, C.; Lavoute, L.; Gaponov, D.; Hideur, A.; Dumas, P.; Février, S. Supercontinuum-based Fourier transform infrared spectromicroscopy. *Optica* **2018**, *5*, 378–381. [CrossRef]
4. Israelsen, N.M.; Petersen, C.R.; Barh, A.; Jain, D.; Jensen, M.; Hannesschläger, G.; Lichtenberg, P.T.; Pedersen, C.; Podoleanu, A.; Bang, O. Real-time high-resolution mid-infrared optical coherence tomography. *Light Sci. Appl.* **2019**, *8*, 11. [CrossRef]
5. Zorin, I.; Brouczek, D.; Geier, S.; Nohut, S.; Eichelseder, J.; Huss, G.; Schwentenwein, M.; Heise, B. Mid-infrared optical coherence tomography as a method for inspection and quality assurance in ceramics additive manufacturing. *Open Ceram.* **2022**, *12*, 100311. [CrossRef]
6. Jahromi, K.E.; Pan, Q.; Hogstedt, L.; Friis, S.M.M.; Khodabakhsh, A.; Moselund, P.M.; Harren, F.J.M. Mid-infrared supercontinuum-based upconversion detection for trace gas sensing. *Opt. Express* **2019**, *27*, 24469–24480. [CrossRef] [PubMed]
7. Huang, Z.; Li, W.; Cui, Y.; Wang, Z. Efficient mid-infrared cascade Raman source in methane-filled hollow-core fibers operating at 2.8 μm. *Opt. Lett.* **2018**, *43*, 4671–4674.
8. Cao, L.; Gao, S.; Peng, Z.; Wang, X.; Wang, Y.; Wang, P. High peak power 2.8 μm Raman laser in a methane-filled negative-curvature fiber. *Opt. Express* **2018**, *26*, 5609–5615. [CrossRef]
9. Lanari, A.M.; Mulvad, H.C.H.; Mousavi, S.M.A.; Davidson, I.A.; Fu, Q.; Norak, P.; Richardson, D.J.; Poletti, F. High power Raman second stokes generation in a methane filled hollow core fiber. *Opt. Express* **2023**, *31*, 41191–41201. [CrossRef] [PubMed]
10. Gladyshev, A.; Yatsenko, Y.; Kolyadin, A.; Kompanets, V.; Bufetov, I. Mid-infrared 10-μJ-level sub-picosecond pulse generation via stimulated Raman scattering in a gas-filled revolver fiber. *Opt. Mat. Express* **2020**, *10*, 3081–3089. [CrossRef]
11. Gladyshev, A.; Yatsenko, Y.; Kolyadin, A.; Bufetov, I. Visible to Mid-Infrared Supercontinuum Initiated by Stimulated Raman Scattering of 1.03 μm Ultrashort Pulses in a Gas-Filled Silica Fiber. *Photonics* **2022**, *9*, 997. [CrossRef]
12. Gladyshev, A.V.; Dubrovskii, D.S.; Juravleva, E.E.; Kosolapov, A.F.; Yatsenko, Y.P.; Bufetov, I.A. Raman generation of ps pulses at λ = 3.9 μm in a hollow-core revolver fiber. *Optoelectron. Instrum. Proc.* **2023**, *59*, 10–17. [CrossRef]
13. Sakr, H.; Chen, Y.; Jasion, G.T.; Bradley, T.D.; Hayes, J.R.; Mulvad, H.C.H.; Davidson, I.A.; Fokoua, E.N.; Poletti, F. Hollow core optical fibres with comparable attenuation to silica fibres between 600 and 1100 nm. *Nat. Commun.* **2020**, *11*, 6030. [CrossRef] [PubMed]
14. Belardi, W.; Knight, J.C. Hollow antiresonant fibers with reduced attenuation. *Opt. Lett.* **2014**, *39*, 1853–1855. [CrossRef]
15. Yu, F.; Knight, J.C. Negative curvature hollow-core optical fiber. *IEEE J. Sel. Top. Quantum Electron.* **2016**, *22*, 146–155. [CrossRef]
16. Yu, F.; Song, P.; Wu, D.; Birks, T.; Bird, D.; Knight, J. Attenuation limit of silica-based hollow-core fiber at mid-IR wavelengths. *APL Photonics* **2019**, *4*, 080803. [CrossRef]
17. Fokoua, E.N.; Mousavi, S.A.; Jasion, G.T.; Richardson, D.J.; Poletti, F. Loss in hollow-core optical fibers: Mechanisms, scaling rules, and limits. *Adv. Opt. Photonics* **2023**, *15*, 1–83. [CrossRef]
18. Ding, W.; Wang, Y.Y.; Gao, S.F.; Wang, M.L.; Wang, P. Recent progress in low-loss hollow-core anti-resonant fibers and their applications. *IEEE J. Sel. Top. Quantum Electron.* **2020**, *26*, 1–12. [CrossRef]
19. Chen, Y.; Petrovich, M.N.; Fokoua, E.N.; Adamu, A.I.; Hassan, M.R.A.; Sakr, H.; Slavík, R.; Gorajoobi, S.B.; Alonso, M.; Ando, R.F.; et al. Hollow Core DNANF Optical Fiber with <0.11 dB/km Loss. In Proceedings of the Optical Fiber Communication Conference (OFC), San Diego, CA, USA, 24–28 March 2024. Technical Digest Series (Optica Publishing Group, 2024), paper Th4A.8.
20. Yatsenko, Y.P.; Gladyshev, A.V.; Bufetov, I.A. Coherent mid-IR supercontinuum in a hollow core fiber filled with a mixture of deuterium and nitrogen. *Bull. Lebedev Phys. Inst.* **2023**, *50*, S996–S1005. [CrossRef]
21. Dudley, J.; Taylor, R. *Supercontinuum Generation in Optical Fibers*, 1st ed.; University Press: Cambridge, UK, 2010; pp. 32–52.
22. Chen, Y.; Sidorenko, P.; Antonio-Lopez, E.; Amezcua-Correa, R.; Wise, F. Efficient soliton self-frequency shift in hydrogen-filled hollow-core fiber. *Opt. Lett.* **2022**, *47*, 285–288. [CrossRef]
23. Gao, S.-F.; Wang, Y.-Y.; Belli, F.; Brahms, C.; Wang, P.; Travers, J.C. From Raman frequency combs to supercontinuum generation in nitrogen-filled hollow-core anti-resonant fiber. *Laser Photonics Rev.* **2022**, *16*, 2100426. [CrossRef]
24. Ottush, J.J.; Rockwell, D.A. Measurement of Raman Gain Coefficients of Hydrogen, Deuterium, and Methane. *IEEE J. Quant. Electr.* **1988**, *24*, 2076–2080. [CrossRef]
25. Edwards, H.G.M.; Long, D.A.; Sherwoud, G. Line widths in the pure rotational Raman spectra of hydrogen and deuterium self-broadened and broadened by foreign gases. *J. Raman Spectrosc.* **1991**, *22*, 607–611. [CrossRef]
26. Wahlstrand, J.K.; Zahedpour, S.; Cheng, Y.-H.; Palastro, J.P.; Milchberg, H.M. Absolute measurement of the ultrafast nonlinear electronic and rovibrational response in H_2 and D_2. *Phys. Rev. A* **2015**, *92*, 063828. [CrossRef]

27. Dudley, J.M.; Genty, G.; Coen, S. Supercontinuum generation in photonic crystal fiber. *Rev. Mod. Phys.* **2006**, *78*, 1135–1184. [CrossRef]
28. Benabid, F.; Bouwmans, G.; Knight, J.C.; Russell, P.S.J.; Couny, F. Ultrahigh efficiency laser wavelength conversion in a gas-filled hollow core photonic crystal fiber by pure stimulated rotational Raman scattering in molecular hydrogen. *Phys. Rev. Lett.* **2004**, *93*, 123903. [CrossRef]
29. Couny, F.; Carraz, O.; Benabid, F. Control of transient regime of stimulated Raman scattering using hollow-core PCF. *J. Opt. Soc. Am. B.* **2009**, *26*, 1209–1215. [CrossRef]